Nanoscale

COMMUNICATION

View Article Online
View Journal | View Issue

Cite this: *Nanoscale*, 2019, **11**, 23132

Received 26th August 2019,
Accepted 8th November 2019

DOI: 10.1039/c9nr07365e

rsc.li/nanoscale

Surface state tunable energy and mass renormalization from homothetic quantum dot arrays†

Ignacio Piquero-Zulaica, *[a,b,c] Jun Li,[d] Zakaria M. Abd El-Fattah, [e,f] Leonid Solianyk,[d] Iker Gallardo,[a] Leticia Monjas,[g] Anna K. H. Hirsch, [g,h] Andres Arnau, [a,b,i] J. Enrique Ortega, [a,b,j] Meike Stöhr *[d] and Jorge Lobo-Checa *[k,l]

Quantum dot arrays in the form of molecular nanoporous networks are renowned for modifying the electronic surface properties through quantum confinement. Here we show that, compared to the pristine surface state, the band bottom of the confined states can exhibit downward shifts accompanied by a lowering of the effective masses simultaneous to the appearance of tiny gaps at the Brillouin zone boundaries. We observed these effects by angle resolved photoemission for two self-assembled homothetic (scalable) Co-coordinated metal–organic networks. Complementary scanning tunneling spectroscopy measurements confirmed these findings. Electron plane wave expansion simulations and density functional theory calculations provide insight into the nature of this phenomenon, which we assign to metal–organic overlayer–substrate interactions in the form of adatom–substrate hybridization. To date, the absence of the experimental band structure resulting from single metal adatom coordinated nanoporous networks has precluded the observation of the significant surface state renormalization reported here, which we infer to be general for low interacting and well-defined adatom arrays.

Over the last few decades, the concepts of supramolecular chemistry have been successfully transferred to the construction of two-dimensional (2D) self-assembled molecular arrangements on metallic surfaces.[1–4] By selecting the proper tectons (molecular constituents and, if required, metal linkers) and depositing them onto selected substrates, long-range ordered, regular and robust nanoporous networks have been achieved, ranging from hydrogen-[5] or halogen-bonded,[6] to metal–organic structures.[7,8] Such regular structures stand out as ideal templates for nanopatterning organic and inorganic adsorbates by selective adsorption.[9–14] Nanoporous networks are also referred to as quantum dot (QD) arrays since they can confine surface state (SS) electrons and provide a vast playground for studying and engineering the electronic properties of new and exotic 2D materials. Indeed, metal–organic networks are known to show novel magnetic properties,[15,16] catalytic effects,[17] oxidation states,[18] and exotic tessellation[19–21] and bear the prospect of exhibiting topological electronic bands.[22,23]

The dominant electronic signature around the Fermi level due to the presence of nanoporous networks comes from the substrate's surface state electrons, which scatter at the molecular array and become confined within individual nanopores.[24,25] The tunability of the confined electronic state has so far been achieved by varying the pore dimensions, *i.e.* the QD size.[25,26] However, since the confining potential barriers are not infinite, these QDs are not independent but coupled, as has been shown by angle resolved photoemission

[a]*Centro de Física de Materiales CSIC/UPV-EHU-Materials Physics Center, Manuel Lardizabal 5, E-20018 San Sebastián, Spain. E-mail: ipiquerozulaica@gmail.com*
[b]*Donostia International Physics Center, Paseo Manuel Lardizabal 4, E-20018 Donostia-San Sebastián, Spain*
[c]*Physik Department E20, Technische Universität München, 85748 Garching, Germany*
[d]*Zernike Institute for Advanced Materials, University of Groningen, Nijenborgh 4, 9747 AG Groningen, The Netherlands. E-mail: m.a.stohr@rug.nl*
[e]*Physics Department, Faculty of Science, Al-Azhar University, Nasr City E-11884 Cairo, Egypt*
[f]*ICFO-Institut de Ciencies Fotoniques, The Barcelona Institute of Science and Technology, 08860 Castelldefels, Barcelona, Spain*
[g]*Stratingh Institute for Chemistry, University of Groningen, Nijenborgh 7, 9747 AG Groningen, The Netherlands*
[h]*Department for Drug Design and Optimization, Helmholtz Institute for Pharmaceutical Research Saarland (HIPS) – Helmholtz Centre for Infection Research (HZI), Campus Building E8.1, 66123 Saarbrücken, Germany*
[i]*Dpto. de Física de Materiales, Universidad del País Vasco, E-20018 San Sebastián, Spain*
[j]*Universidad del País Vasco, Dpto. Física Aplicada I, E-20018 San Sebastián, Spain*
[k]*Instituto de Ciencia de Materiales de Aragón (ICMA), CSIC-Universidad de Zaragoza, E-50009 Zaragoza, Spain. E-mail: jorge.lobo@csic.es*
[l]*Departamento de Física de la Materia Condensada, Universidad de Zaragoza, E-50009 Zaragoza, Spain*

†Electronic supplementary information (ESI) available. See DOI: 10.1039/C9NR07365E

spectroscopy (ARPES) through the existence of new dispersive electronic bands[24] as well as by Fourier-transform scanning tunneling spectroscopy (FT-STS) data.[27] These QD array bands can be modified through the condensation of guest atoms[28] or by changing the barrier width.[6] The standard fingerprints, whenever the confinement of two-dimensional electron gases (2DEGs) occurs on noble metal surfaces, are in the form of an energy shift of their band bottom towards the Fermi level, an increase of the effective mass, and the appearance of energy gaps at the surface Brillouin zone (BZ) boundaries.[6,24,29,30]

In this work we show for two homothetic (scalable) metal–organic nanoporous networks (MONNs) grown on Au(111) the first experimental evidence of energy downshifts and reduced effective masses compared to the pristine SS, simultaneous to the opening of zone boundary gaps that suggest electron confinement within the nanocavities. More specifically, these effects are gradual, *i.e.* they depend on the network dimensions. The interaction between the Au substrate and the MONNs is at the base of these unexpected phenomena and not a consequence of the quantum confinement.

The studied scalable Co-coordinated networks were grown on Au(111) from two related dicarbonitrile-polyphenyl derivatives. Specifically, we used dicarbonitrile-terphenyl (Ph3) and dicarbonitrile-hexaphenyl (Ph6) molecules and Co atoms in a 3 : 2 stoichiometry to fabricate the MONNs. These tectons were sequentially evaporated (molecules first, then Co) onto Au(111) followed by a mild annealing to 400 K. This resulted in two scalable, periodic, long-range ordered and practically defect free QD arrays [shown in Fig. 1(A and B)] and named hereafter Ph6Co and Ph3Co. In agreement with previous work,[25] the networks exhibit sixfold symmetry with unit cell vectors of 3.53 nm (for Ph3Co) and 5.78 nm (for Ph6Co) along the [11$\bar{2}$] direction and enclose pore areas of 8 nm^2 and 24 nm^2, respectively. Note that the interaction of both networks with the substrate is assumed to be rather weak since the herringbone reconstruction is neither lifted nor modified in its periodicity (see Fig. S1†).[31] We experimentally probed these networks with ARPES [helium I source (h/ν = 21.2 eV) at 150 K] and scanning tunneling microscopy/spectroscopy (STM/STS) at 5 K to obtain both spatially averaged and spatially highly resolved information (ESI†). The experimental data are complemented by Electron Plane Wave Expansion (EPWE) simulations and Density Functional Theory (DFT) calculations (experimental and theoretical methods described in the ESI†).

The 2DEG onset of Ph6Co and Ph3Co networks formed on Au(111) is reliably determined by ARPES and only approximately by STS.[6] Moreover, ARPES – in contrast to STS – can resolve the QD array band structure from a MONN. However, this can be exceedingly challenging because the networks must be extended, almost defect-free and completely covering the probed surface (in the absence of other coexisting molecular phases).[6,24] To achieve these conditions we evaporated the molecules and Co adatoms in orthogonal shallow gradient depositions on the Au(111) substrate, thereby ensuring the

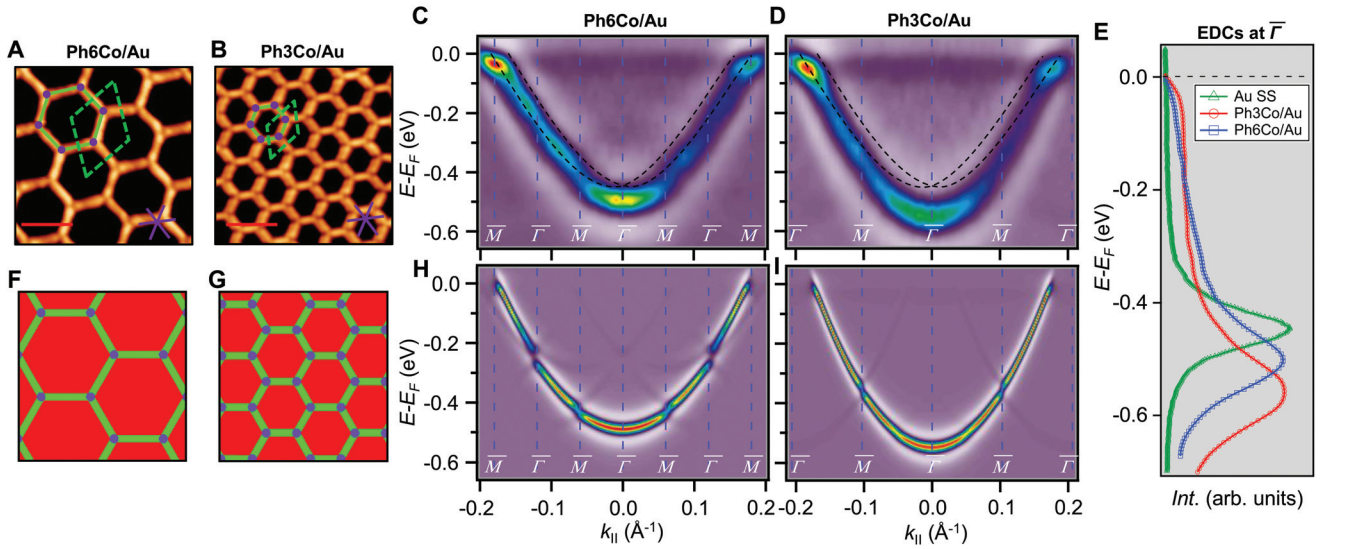

Fig. 1 STM topographies of the single domain Co-coordinated hexagonal QD arrays using (A) dicarbonitrile-hexaphenyl (Ph6) and (B) dicarbonitrile-terphenyl (Ph3). Scale bar in red corresponds to 5 nm. The high symmetry directions and corresponding unit cells [with unit vectors 5.78 nm (for Ph6Co) and 3.53 nm (for Ph3Co)] are shown in the images (STM parameters: (A) V = −0.50 V, I_t = 150 pA; (B) V = −0.23 V, I_t = 250 pA). (C and D) Second derivative of the spectral density obtained by ARPES at 150 K along the $\overline{\Gamma M}$ high-symmetry direction for both Ph6Co and Ph3Co nanoporous networks. The band structures exhibit downward shifts of the band bottom and gap openings (clearly visualized in Fig. S2†) at the superstructure symmetry points compared to the pristine Au(111) Shockley state (black dotted lines). (E) Energy distribution curves (EDCs) at normal emission ($\overline{\Gamma}$ point) for pristine Au(111) (green), Ph6Co (blue) and Ph3Co (red). A gradual downshift of the band bottom as the pore size is reduced (ΔE_{Ph6Co} = 40 meV and ΔE_{Ph3Co} = 100 meV with respect to the Au SS) are found. (F and G) 2D potential geometry used for the EPWE modelization, where green stands for the molecular repulsive potentials, purple for slightly repulsive Co regions and red for cavity regions with zero potential. (H and I) Band structure along the $\overline{\Gamma M}$ direction of the overlayers simulated by EPWE based on the previous geometry. Matching the experimental ARPES data (gap openings and band-bottom shifts) requires a significant modification of the 2DEG energy reference (see text for details).

Table 1 ARPES experimental binding energies at $\bar{\Gamma}$ and effective masses (columns $E_B^{\bar{\Gamma}}$ and m^*/m_0) for the substrate and the two networks. The corresponding 2DEG references (band bottom energy and effective masses) required for matching ARPES with the EPWE simulations are indicated in the last two columns: $E_{EPWE}^{Ref,\bar{\Gamma}}$ and $m_{EPWE}^{*,Ref}/m_0$

	$E_B^{\bar{\Gamma}}$ (eV)	m^*/m_0	$E_{EPWE}^{Ref,\bar{\Gamma}}$ (eV)	$m_{EPWE}^{*,Ref}/m_0$
Au(111)	0.45	0.255	0.45	0.26
Ph6Co	0.49	0.24	0.52	0.24
Ph3Co	0.55	0.22	0.59	0.21

existence of an area with optimal coverage and the exact 3 : 2 stoichiometry (*cf.* ESI†).[32] Fig. 1(C and D) shows the second derivative of the ARPES spectral density from Ph6Co and Ph3Co along the $\overline{\Gamma M}$ high symmetry direction (see also Fig. S2†). We observed a gradual downshift of the band bottom ($\bar{\Gamma}$ point) towards higher binding energies as the pore size is reduced, which can be quantified from the normal emission energy distribution curves (EDCs) [*cf.* Fig. 1(E) and Table 1]. Note that this clearly goes in the opposite direction to the energy shift expected from conventional lateral confinement systems (and does not relate to the single components shown in Fig. S3†). Simultaneous to this downshift, we observed a reduction of the effective mass (see Table 1), resembling a Fermi wave-vector pinning (see Fig. S2†). The partial confinement of the substrate's 2DEG is inferred from the presence of small gaps (observed as slight intensity variations) at the symmetry points, which denotes weak scattering from the network barriers. The fact that our experimental dataset does not show spin–orbit splitting for Ph3Co and Ph6Co does not imply its absence, as it might be masked by the ARPES lineshape broadening due to network imperfections and our limited experimental resolution (ESI†).[33]

To unravel the potential energy landscapes generated by the molecular networks and their confining properties, we performed EPWE simulations. Such a semi-empirical model has been successfully used for similar systems.[6,25,34] The geometries of both systems for the simulations were defined following topographic STM images [see Fig. 1(F and G)]. Assuming repulsive scattering potential sites for molecules (V_{mol} = 250 meV) and Co atoms (V_{Co} = 50 meV), the experimental data were correctly reproduced. In particular, the ARPES energy gaps (~25 meV for Ph6Co and ~30 meV for Ph3Co at $\bar{M}$) reflect the weak scattering strength of the networks [Fig. 1(H and I)]. However, such repulsive scattering is known to shift the 2DEG band bottom (at $\bar{\Gamma}$) upwards, opposite to what is observed here. In this way, the ARPES dispersions can only be matched by EPWE when adopting higher binding energy references and smaller effective masses than the pristine Au(111) SS (see Table 1). In other words, using the original dispersion of the Au(111) SS as a scattering reference cannot correctly reproduce the experimental data.

Such an unexpected scenario questions the confining capabilities of these MONNs. Using STS, we could verify that these networks do confine the Au SS, similar to the ones generated onto Ag(111) by the same family of molecules.[25] In the center

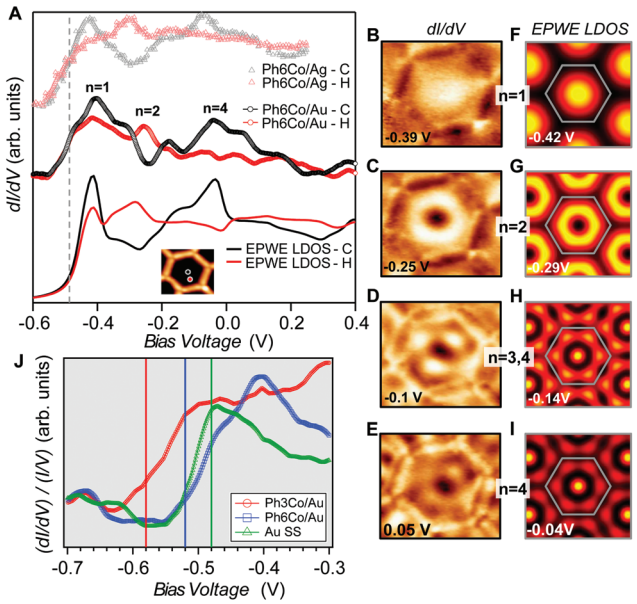

Fig. 2 Local confinement and renormalization effects observed by STM/STS. (A) d*I*/d*V* spectra at the pore center (black) and halfway (red) for three Ph6Co datasets: Experimental curves of Ph6Co on Au(111) (middle), corresponding EPWE conductance simulation using the ARPES parameters (bottom), and experimental spectra of Ph6Co on Ag(111) adapted from ref. 25 and normalized (see the text) to the Au(111) 2DEG (top). The spectra are made up of the characteristic confined state resonances that alternate depending on the wavefunction spatial distribution, *i.e.*, n = 1 and n = 4 peak at the pore center and n = 2 at halfway.[14,35] (B to E) Experimental d*I*/d*V* maps reproducing standing wave patterns of the different energy levels n showing excellent agreement with the EPWE simulated ones at similar energies (F to I). The observed deviations for the higher energy conductance maps can be assigned to weak potential alterations stemming from the underlying herringbone reconstruction (see Fig. S1†), which are not considered in the simulations (see text for details). (J) Zoom-in onto the experimental d*I*/d*V* onset for the pristine Au(111) SS (green) and Ph6Co (blue) and Ph3Co (red) networks probed at the center of the pores. For comparison, vertical lines marking the bottom energy position found in ARPES (temperature corrected by 30 meV) are included in the panel. The STS onsets are in close proximity to these vertical lines.

of Fig. 2(A) we present the Ph6Co STS data acquired at two different positions. The conductance spectra together with the d*I*/d*V* maps taken at different voltages [Fig. 2(B–E)] exhibit clear confinement resonances within the pores.[6,14,24,25,28,34] Such electron localization mirrors the one observed for the same network on Ag(111).[25] In order to directly compare them we adapt the d*I*/d*V* spectra in ref. 25 by normalizing the energy axis by the ratio of the respective effective masses $\left(m_{Ag}^{*,Ph6Co}/m_{Au}^{*,Ph6Co} = 0.41/0.24\right)$ and shifting the onset of the Ag SS to the one of Au (−485 meV at 5 K). The agreement (lineshape and peak energies) between the two datasets is quite reasonable [*cf.* middle and top of Fig. 2(A)], demonstrating that the confinement properties of Ph6Co are similar for the two substrates.

We can now address the 2DEG energy downshift with respect to the Au SS upon network formation using local techniques. The overall d*I*/d*V* lineshapes at the pore center exhibit

broad peak widths (reflecting the ARPES bandwidth) and are quite asymmetric (with maxima being displaced towards higher energy).[6,49] Such spectral asymmetry for $n = 1$ at the pore center can be understood from a band structure perspective: the reduced onset contribution relates to electrons spreading out over the surface given their longer wavelength ($\lambda = 2\pi/k$) at the band bottom ($k \sim 0$ around $\bar{\Gamma}$). Contrarily, STS is maximized at higher energies (close to the $\bar{M}$ point) since the electrons have much shorter wavelengths, thereby becoming much more sensitive to the network barriers and prone to be trapped within the pores. Fig. 2(J) shows the STS spectra of the two networks at the pore center compared to the Au(111) SS. For Ph3Co the onset is clearly shifted away from the Au SS onset, whereas for Ph6Co it is similar but still slightly displaced. This is also the case for these networks on Ag(111) (see Fig. S4†). For Ph6Co, we simulated the STS point spectra and conductance maps [Fig. 2(A and F–I)] using the same scattering parameters and effective mass reduction as described above for the ARPES electron bands. While the experimental and simulated STS spectra match reasonably well, we observe slight discrepancies for the conductance maps obtained at higher energies. This can be ascribed to weak potential variations introduced by the reconstruction of the underlying substrate. Indeed the Ph6Co unit cell is large enough to host both fcc and hcp regions within a single pore (*cf.* Fig. S1†), which was not accounted for by the EPWE simulations.

In essence, the STS shifts qualitatively agree with the ARPES results, as observed in Fig. 2(J) (vertical lines), supporting a change in the 2DEG reference upon the network presence on the surface. Such subtle downward energy shifts, as is the case of Ph3Co and Ph6Co, also exist for other single atom coordinated MONNs (see Fig. S5†). However, the present effect has not been reported up to now because complementary photoemission experiments are required for determining this 2DEG onset reference.

Different factors might be responsible for these counterintuitive downward energy shifts of the confined states with respect to the Au SS. This effect can be attributed to the network–substrate interactions in the form of charge transfer (doping effects), localized bound states or hybridization effects of the metal adsorbates that renormalize the 2DEG that is modulated by the network potential landscape. As the shift is gradual, being larger for Ph3Co than for Ph6Co, and the networks are homothetic, it could be induced by charge transfer from the Co adatoms [full surface coverage of Ph3Co/Ph6Co corresponds to 0.015/0.005 monolayers (ML) of Co] to the Au SS, similar to the downshift induced by alkali metals.[36] However, the fact that m^* decreases and the Fermi wavevector (k_F) is practically pinned suggests the conservation of the 2DEG electron occupancy (the electron density $n = \frac{k_F^2}{2\pi}$).[37,38] Therefore, the Au SS shift is not driven by electron charge transfer from the Co atom to the Au surface.

Localized bound states directly below the Co atoms could also be the reason for this downshift. Bound states result from localized attractive perturbations of an atom on a 2DEG[39] giving rise to a split resonance with its bonding state shifted to lower energies with respect to the pristine SS band edge.[40–42] However, our Co adatom STS spectrum does not show the distinctive feature (peak below the SS onset) in its lineshape, nor the modulation with distance close to the SS onset that are expected for these states (*cf.* Fig. S6†). The same situation occurs when this MONN family has been grown on Ag(111).[25] Moreover, our ARPES band structure (Fig. S2†) is qualitatively similar to the QD array cases for porous networks without coordinating adatoms,[6] which clearly differs from the bound state vertically split band structure observed for a random distribution of Au adatoms.[38] All these facts discard the bound states of the coordinating atoms as the cause for this effect.

Finally, we consider the Co interaction with the Au substrate, that is, the local Co/Au hybridization.[43] For this, we explore the weak Co–Au hybridization by means of DFT calculations of Co atom arrays onto a non-reconstructed Au(111) surface. Fig. 3 shows the calculated band structure from two selected supercells: 2 × 2 (0.25 ML) on the left and 3 × 3 (0.11 ML) on the right. These superstructures introduce an evident difference in the folding of the Au bands (in black), but more

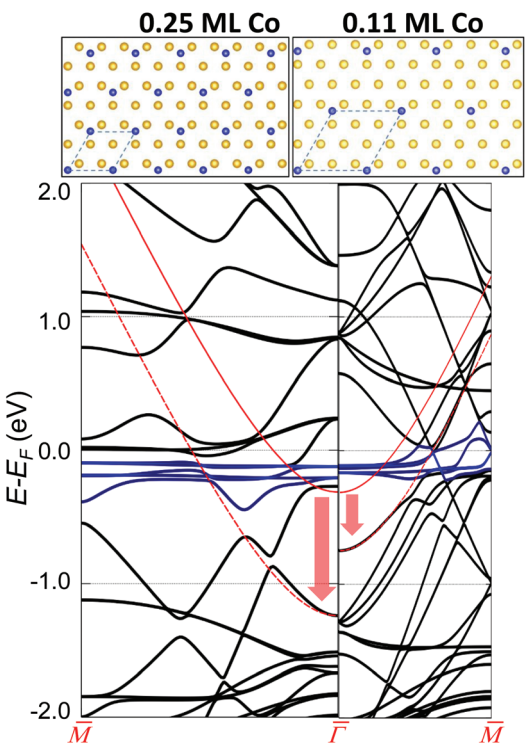

Fig. 3 Visualization of the Au(111) surface state (continuous red curve for the pristine case) downward energy shift at two different Co coverages. The vertical arrows show the calculated shift close to $\bar{\Gamma}$ and the red dotted lines are a guide to the eye to follow the altered SS. The left panel corresponds to 0.25 ML of Co and the right panel to 0.11 ML, as obtained using a 2 × 2 and a 3 × 3 surface unit cell that are shown on top. The different supercells introduce an evident difference in the folding of the Au bands. The blue curves near the Fermi level correspond to Co d-bands. The coupling between the Co d-bands and folded bulk-bands with the Au(111) surface state pushes it downwards in energy, the shift being larger at higher Co coverages.

importantly, a clear downshift of the pristine Au SS (red arrow). We find that the magnitude of the downshift is directly related to the amount of isolated Co adatoms on the surface (Table S1†). The actual Co coverage within the networks is much lower (by about an order of magnitude), so the expected shift obtained by simple extrapolation to the corresponding Co coverage (of the order of 50 meV) is comparable to the experimental observations (Table S1†). Although geometrical variations (vertical displacements) of the overlayers[7,44,45] that could affect the SS reference cannot be completely discarded, the hybridization (coupling) of the Co d-bands (shown in blue in Fig. 3) and folded bulk-bands with the Au(111) SS convincingly explains the observed SS renormalization effect.[38,50]

This effect turns out to be more general than initially expected. First, because it is likewise observed for this and other families of MONNs grown onto other noble metal substrates (Fig. S5†), and second since additional DFT calculations for homoatomic arrays [Cu/Cu(111) and Au/Au(111)] predict the same effect (Fig. S7†). We deduce that this holds for single (homo- and hetero-) atomic arrays formed onto noble metal substrates whenever the hybridization is weak (physisorption cases), such that the SS character is maintained. Although the modification of the 2DEG does not depend on the network symmetry (see Fig. S5†), the molecule presence is required since it ultimately defines the interaction of the adatom array with the substrate and the adatom concentration defines the energy shift. This scenario commonly applies to MONNs since the adsorption height of adatoms increases due to the coordination with the molecules,[7,44–46] effectively reducing their interaction with the substrate.

Interestingly, this surface state energy downshift is not observed for the case of the DPDI-Cu MONN formed on Cu(111).[24] We infer that such a difference relates to the number of adatoms at coordinating sites (three for the case of DPDI-Cu) that are prone to be less efficiently uplifted from the surface[7] compared to single atom coordinated MONNs. In consequence, the interaction with the underlying substrate would be stronger, leading to higher effective scattering potentials at the coordinating sites, as obtained by EPWE simulations ($V_{\text{Cu trimers-DPDI}} = 390 \pm 50$ meV *vs.* $V_{\text{Co-PhXCo}} = 50$ meV).[47]

In summary, ARPES and STS results reveal a gradual energy and mass renormalization of the Au(111) SS upon the formation of two homothetic single Co coordinated metal–organic networks. EPWE simulations only agree with the experimental data after the 2DEG reference is shifted to higher binding energies. Notably this downshift is gradual with decreasing pore size and is observable in spite of the confining attributes of the nanocavities (that upshifts the states). Our EPWE simulations can satisfactorily match our experimental data using repulsive potentials for both molecules and Co atoms. Overlayer–substrate interactions must be responsible for such counterintuitive effects upon the Au SS reference. Hybridization between the Co adatoms and the folded substrate bands with the Au SS appears as the most plausible cause, as deduced from DFT calculations. We predict that other single atom coordinated MONNs grown on noble metal surfaces should show such subtle counterintuitive 2DEG energy renormalization whenever the SS character is preserved, *i.e.* for weak coupling cases.

Author contribution

I.P-Z., J.E.O. and J.L-C. conducted the ARPES measurements and data analysis; J.L., L.S. and M.S. performed the STM/STS experiments and analysis; Z.M.A.E-F. performed the EPWE simulations; I.G. and A.A. performed the DFT calculations; L. M. and A.K.H.H. synthesized the molecules; I.P-Z. and J.L-C. wrote the manuscript. All authors contributed to the revision and final discussion of the manuscript; I.P-Z., M.S. and J.L-C. conceived this project.

Conflicts of interest

The authors declare that no conflicts of interest exist.

Acknowledgements

We acknowledge Prof. J. García de Abajo for providing the EPWE code and the financial support from the Spanish Ministry of Economy, Industry and Competitiveness (MINECO, Grant No. MAT2016-78293-C6 and FIS2016-75862-P), from the Basque Government (Grant No. IT-1255-19 and IT-756-13), from the Regional Government of Aragon (RASMIA project), from the European Regional Development Fund (ERDF) under the program Interreg V-A España-Francia-Andorra (Contract No. EFA 194/16 TNSI) and from the European Research Council (ERC-2012-StG 307760-SURFPRO). The CSIC Open Access Publication Support Initiative through its Unit of Information Resources for Research (URICI) is gratefully acknowledged.

References

1 J.-M. V. Lehn, *Supramolecular Chemistry, Concepts and Perspectives*, VCH, Weinheim, 1995.
2 J. L. Atwood, J. E. D. Davies, D. D. MacNicol, F. Vögtle and J.-M. V. Lehn, *Comprehensive Supramolecular Chemistry*, Pergamon, New York, 1996.
3 S. Stepanow, N. Lin and J. V. Barth, *J. Phys.: Condens. Matter*, 2008, **20**, 184002.
4 K. Müller, M. Enache and M. Stöhr, *J. Phys.: Condens. Matter*, 2016, **28**, 153003.
5 G. Pawin, K. L. Wong, K.-Y. Kwon and L. Bartels, *Science*, 2006, **313**, 961.
6 I. Piquero-Zulaica, J. Lobo-Checa, A. Sadeghi, Z. M. Abd El-Fattah, C. Mitsui, T. Okamoto, R. Pawlak, T. Meier, A. Arnau, J. E. Ortega, J. Takeya, S. Goedecker, E. Meyer and S. Kawai, *Nat. Commun.*, 2017, **8**, 787.

7 M. Matena, J. Björk, M. Wahl, T.-L. Lee, J. Zegenhagen, L. H. Gade, T. A. Jung, M. Persson and M. Stöhr, *Phys. Rev. B: Condens. Matter Mater. Phys.*, 2014, **90**, 125408.
8 L. Dong, Z. Gao and N. Lin, *Prog. Surf. Sci.*, 2016, **91**, 101.
9 M. Stöhr, M. Wahl, H. Spillmann, L. H. Gade and T. A. Jung, *Small*, 2007, **3**, 1336.
10 Z. Cheng, J. Wyrick, M. Luo, D. Sun, D. Kim, Y. Zhu, W. Lu, K. Kim, T. L. Einstein and L. Bartels, *Phys. Rev. Lett.*, 2010, **105**, 066104.
11 J. Wyrick, D.-H. Kim, D. Sun, Z. Cheng, W. Lu, Y. Zhu, K. Berland, Y. S. Kim, E. Rotenberg, M. Luo, P. Hyldgaard, T. L. Einstein and L. Bartels, *Nano Lett.*, 2011, **11**, 2944.
12 S. Nowakowska, A. Wäckerlin, S. Kawai, T. Ivas, J. Nowakowski, S. Fatayer, C. Wäckerlin, T. Nijs, E. Meyer, J. Björk, M. Stöhr, L. H. Gade and T. A. Jung, *Nat. Commun.*, 2015, **6**, 6071.
13 R. Zhang, G. Lyu, C. Chen, T. Lin, J. Liu, P. N. Liu and N. Lin, *ACS Nano*, 2015, **9**, 8547.
14 M. Pivetta, G. E. Pacchioni, U. Schlickum, J. V. Barth and H. Brune, *Phys. Rev. Lett.*, 2013, **110**, 086102.
15 N. Abdurakhmanova, T.-C. Tseng, A. Langner, C. S. Kley, V. Sessi, S. Stepanow and K. Kern, *Phys. Rev. Lett.*, 2013, **110**, 027202.
16 T. R. Umbach, M. Bernien, C. F. Hermanns, A. Krüger, V. Sessi, I. Fernandez-Torrente, P. Stoll, J. I. Pascual, K. J. Franke and W. Kuch, *Phys. Rev. Lett.*, 2012, **109**, 267207.
17 R. Gutzler, S. Stepanow, D. Grumelli, M. Lingenfelder and K. Kern, *Acc. Chem. Res.*, 2015, **48**, 2132.
18 Y. Li, J. Xiao, T. E. Shubina, M. Chen, Z. Shi, M. Schmid, H.-P. Steinrück, J. M. Gottfried and N. Lin, *J. Am. Chem. Soc.*, 2012, **134**, 6401.
19 J. I. Urgel, D. Écija, G. Lyu, R. Zhang, C.-A. Palma, W. Auwärter, N. Lin and J. V. Barth, *Nat. Chem.*, 2016, **8**, 657.
20 L. Yan, G. Kuang, Q. Zhang, X. Shang, P. N. Liu and N. Lin, *Faraday Discuss.*, 2017, **204**, 111.
21 Y.-Q. Zhang, M. Paszkiewicz, P. Du, L. Zhang, T. Lin, Z. Chen, S. Klyatskaya, M. Ruben, A. P. Seitsonen, J. V. Barth and F. Klappenberger, *Nat. Chem.*, 2018, **10**, 296.
22 X. Zhang and M. Zhao, *Sci. Rep.*, 2015, **5**, 14098.
23 L. Z. Zhang, Z. F. Wang, B. Huang, B. Cui, Z. Wang, S. X. Du, H.-J. Gao and F. Liu, *Nano Lett.*, 2016, **16**, 2072.
24 J. Lobo-Checa, M. Matena, K. Müller, J. H. Dil, F. Meier, L. H. Gade, T. A. Jung and M. Stöhr, *Science*, 2009, **325**, 300.
25 F. Klappenberger, D. Kühne, W. Krenner, I. Silanes, A. Arnau, F. J. García de Abajo, S. Klyatskaya, M. Ruben and J. V. Barth, *Phys. Rev. Lett.*, 2011, **106**, 026802.
26 A. Shchyrba, S. C. Martens, C. Wäckerlin, M. Matena, T. Ivas, H. Wadepohl, M. Stöhr, T. A. Jung and L. H. Gade, *Chem. Commun.*, 2014, **50**, 7628.
27 S. Wang, W. Wang, L. Z. Tan, X. G. Li, Z. Shi, G. Kuang, P. N. Liu, S. G. Louie and N. Lin, *Phys. Rev. B: Condens. Matter Mater. Phys.*, 2013, **88**, 245430.
28 S. Nowakowska, A. Wäckerlin, I. Piquero-Zulaica, J. Nowakowski, S. Kawai, C. Wäckerlin, M. Matena, T. Nijs, S. Fatayer, O. Popova, *et al.*, *Small*, 2016, **12**, 3757.
29 A. Mugarza, F. Schiller, J. Kuntze, J. Cordón, M. Ruiz-Osés and J. E. Ortega, *J. Phys.: Condens. Matter*, 2006, **18**, S27–S49.
30 A. Bendounan, F. Forster, J. Ziroff, F. Schmitt and F. Reinert, *Surf. Sci.*, 2006, **600**, 3865.
31 M. Ruiz-Osés, D. G. de Oteyza, I. Fernández-Torrente, N. Gonzalez-Lakunza, P. M. Schmidt-Weber, T. Kampen, K. Horn, A. Gourdon, A. Arnau and J. E. Ortega, *ChemPhysChem*, 2009, **10**, 896.
32 I. Piquero-Zulaica, S. Nowakowska, J. E. Ortega, M. Stöhr, L. H. Gade, T. A. Jung and J. Lobo-Checa, *Appl. Surf. Sci.*, 2017, **391**, 39.
33 J. Lobo-Checa, F. Meier, J. H. Dil, T. Okuda, M. Corso, V. N. Petrov, M. Hengsberger, L. Patthey and J. Osterwalder, *Phys. Rev. Lett.*, 2010, **104**, 187602.
34 F. Klappenberger, D. Kühne, W. Krenner, I. Silanes, A. Arnau, F. J. García de Abajo, S. Klyatskaya, M. Ruben and J. V. Barth, *Nano Lett.*, 2009, **9**, 3509.
35 J. Li, W.-D. Schneider, S. Crampin and R. Berndt, *Surf. Sci.*, 1999, **422**, 95.
36 E. Bertel and N. Memmel, *Appl. Phys. A: Mater. Sci. Process.*, 1996, **63**, 523.
37 F. Forster, A. Bendounan, J. Ziroff and F. Reinert, *Surf. Sci.*, 2006, **600**, 3870.
38 C. Liu, I. Matsuda, R. Hobara and S. Hasegawa, *Phys. Rev. Lett.*, 2006, **96**, 036803.
39 B. Simon, *Ann. Phys.*, 1976, **97**, 279.
40 V. Madhavan, W. Chen, T. Jamneala, M. F. Crommie and N. S. Wingreen, *Phys. Rev. B: Condens. Matter Mater. Phys.*, 2001, **64**, 165412.
41 F. E. Olsson, M. Persson, A. G. Borisov, J.-P. Gauyacq, J. Lagoute and S. Fölsch, *Phys. Rev. Lett.*, 2004, **93**, 206803.
42 L. Limot, E. Pehlke, J. Kröger and R. Berndt, *Phys. Rev. Lett.*, 2005, **94**, 036805.
43 U. Schlickum, R. Decker, F. Klappenberger, G. Zoppellaro, S. Klyatskaya, M. Ruben, I. Silanes, A. Arnau, K. Kern, H. Brune and J. V. Barth, *Nano Lett.*, 2007, **7**, 3813.
44 Y.-L. Zhao, W. Wang, F. Qi, J.-F. Li, G. Kuang, R.-Q. Zhang, N. Lin and M. A. Van Hove, *Langmuir*, 2017, **33**, 451.
45 Q. Sun, L. Cai, H. Ma, C. Yuan and W. Xu, *ACS Nano*, 2016, **10**, 7023.
46 M. N. Faraggi, V. N. Golovach, S. Stepanow, T.-C. Tseng, N. Abdurakhmanova, C. S. Kley, A. Langner, V. Sessi, K. Kern and A. Arnau, *J. Phys. Chem. C*, 2015, **119**, 547.
47 I. Piquero-Zulaica, Z. M. Abd El-Fattah, O. Popova, S. Kawai, S. Nowakowska, M. Matena, M. Enache, M. Stöhr, A. Tejeda, A. Taleb, E. Meyer, J. E. Ortega, L. H. Gade, T. A. Jung and J. Lobo-Checa, *New J. Phys.*, 2019, **21**, 053004.
48 K. Seufert, W. Auwärter, F. J. Garcıia de Abajo, D. Ecija, S. Vijayaraghavan, S. Joshi and J. V. Barth, *Nano Lett.*, 2013, **13**, 6130.
49 Arrays of coupled QDs give rise to bonding and antibonding continuum states. The minimum energy is established by the bonding state and the overall bandwidth (pro-

portional to the QD intercoupling) is defined by the anti-bonding ones.[48] The STS technique reveals an enhanced sensitivity to probe the anti-bonding state since the wave-function shape for the bonding state is more spread out than the anti-bonding one.[48] Consequently, the peak line-shapes are generally asymmetric with maxima displaced towards the top of the band, which in ARPES matches the $\bar{M}$ point energy.

50 The effect of a Co network on the Au Shockley state cannot be tested with ARPES, since at low coverages Co atoms aggregate forming clusters at herring-bone elbows (see Fig. S3†).

Electronic Supplementary Information: Surface state tunable energy and mass renormalization from homothetic Quantum dot arrays

Ignacio Piquero-Zulaica, Jun Li, Zakaria M. Abd El-Fattah, Leonid Solianyk, Iker Gallardo, Leticia Monjas, Anna K. H. Hirsch, Andres Arnau, J. Enrique Ortega, Meike Stöhr, and Jorge Lobo-Checa

EXPERIMENTAL & THEORETICAL METHODS

ARPES measurements. The Au(111) substrate was prepared by standard cycles of sputtering-annealing at 1 kV and 800 K. The molecules [dicyano sexyphenyl (Ph6) and dicyano terphenyl (Ph3)] were first thermally deposited onto the Au(111) crystal at room temperature from a quartz Knudsen cell and then the Co adatoms, followed by a mild annealing to 400 K. For the ARPES measurements, we evaporated the molecules and the Co adatoms in two orthogonal shallow deposition wedges using a fixed square mask while moving the sample laterally and vertically with a velocity controlled motor to obtain a region with exact 3:2 stoichiometry. Prior to forming this wedge we roughly determine the evaporation parameters for a full surface coverage of the MONN (checked using RT-STM). Afterwards, we apply the gradient method and use shallow deposition coverage wedges [1] in order to perform position dependent ARPES. Our ARPES 2D detector allows us to trace the electronic structure modification around the band bottom where we look for the sharpest 2DEG signal that in this case includes changes in the bottom energy, intensity modulations at the zone boundaries, and side replicas with respect to the pristine case.

The ARPES measurements were performed with a lab-based experimental setup using a display-type hemispherical electron analyzer (SPECS Phoibos 150, energy/angle resolution of 40 meV/0.1°) combined with a monochromatized Helium I source ($h\nu$=21.2 eV). Measurements were acquired with the sample at 150 K by moving the polar angle.

STM measurements. The experiments were carried out in a two-chamber ultrahigh vacuum system (base pressure of 4×10^{-11} mbar) housing a commercial low temperature STM (Scienta Omicron GmbH). The Au(111) substrate was cleaned by repeated cycles of Argon ion sputtering followed by annealing at 800 K. The Ph3 (Ph6) molecules were heated to 445 K (550K) inside a commercial molecule evaporator (OmniVac) and deposited onto the Au(111) substrate held at room temperature. The Co atoms were deposited with an electron beam evaporator (Oxford Applied Research Ltd). STM measurements were performed at both 77 K and 4.5 K with a mechanically cut Pt/Ir wire in constant current mode. All bias voltages are given with respect to a grounded tip. The STM images were processed with the WSxM

software [2]. STS measurements were performed at 4.5 K by using a lock-in amplifier (typical modulation parameters used: amplitude of 10 mV (rms) and frequency of 677 Hz).

EPWE simulations. The combined Plane Wave Expansion (PWE) and Electron Boundary Element Method (EBEM) have been developed by García de Abajo and represent a scalar variant of the electromagnetic PWE/BEM extensively used for solving Maxwell's equation and optical response for arbitrary shapes. It is based on Green's functions for finite geometries and electron plane wave expansion for periodic systems. For the band structure calculations, particle-in-a-box model is extended to infinite 2D systems by defining an elementary cell and using periodic boundary conditions. Within PWE code, solutions of the Schrödinger equation are represented as a linear combination of plane waves and a satisfactory convergence was achieved with a basis set consisting of ~ 100 waves. More information can be found in [3, 4].

DFT calculations. Density Functional Theory calculations have been performed using the VASP code [5–7]. The interaction of the valence electrons with the ion cores was described with the projector augmented wave method (PAW) and the Perdew-Burke-Ernzerhof [8] exchange-correlation functional was used. An energy cutoff of 300 eV in the plane wave expansions and different K-point samplings, depending on the size of the surface unit cells, were employed and checked to be well-converged. A four layer Au(111) slab with hydrogen atoms passivating one of the two vacuum-metal interfaces was used to model the Au(111) surface state [9], while a Co atom was placed on the other interface at 2.5 Angstroms vertical distance at a fcc hollow site. At this distance the Co-Au(111) interaction is weaker than for the optimal adsorption distance but it is the way we mimic a less reactive Co atom in the metal-organic network. Table I summarizes the SS band bottom energies as function of adatom concentration obtained from these calculations.

SUPPLEMENTARY TABLE

Adatom concentration	Array size	Co/Au(111) $\Delta E_{SS}(eV)$	Au/Au(111) $\Delta E_{SS}(eV)$	Cu/Cu(111) $\Delta E_{SS}(eV)$
0.25 ML	2x2	-0.94	-0.92	-0.93
0.17 ML	3x2	-0.70	-0.65	-0.78
0.11 ML	3x3	-0.49	-0.49	-0.35
0.08 ML	3x4	-0.54	–	–

Table S I: Energy shift of the pristine SS with adatom concentration and array size obtained from our DFT calculations. The calculations, from left to right, correspond to the cases of Co/Au(111), Au/Au(111) and Cu/Cu(111). To account for the decoupling effect of the molecules, the adatoms are relaxed at $\sim$ 2.5 Å above the unreconstructed pristine surfaces. The calculations show a general increasing downward shift of the SS with adatom content. Note that the experimental amounts of Co used are significantly lower, corresponding to 0.015 ML for Ph3Co and 0.005 ML for Ph6Co.

SUPPLEMENTARY FIGURES

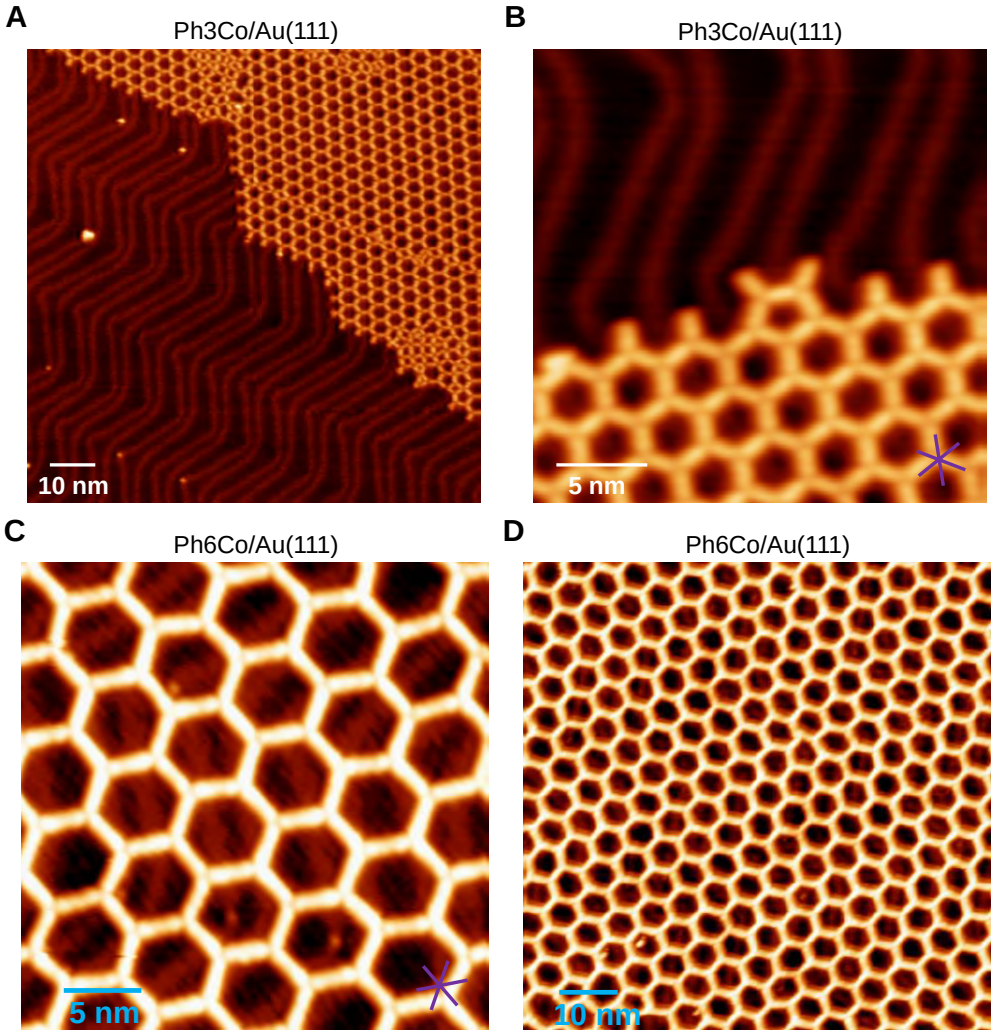

Figure S 1: The herringbone reconstruction of Au is preserved under the Ph3Co and Ph6Co networks, which is an indication of the low interaction between molecules and substrate [10, 11]. (**A**) 100 nm x 100 nm STM image of Ph3Co network on Au(111) at 77 K. This image highlights the growth of the Ph3Co network 30° rotated from $[1\bar{1}0]$ direction of the surface as well as domain boundaries among molecular islands. STM parameters: V=-2 V, I=20 pA. (**B**) 25 nm x 25 nm STM close up image of Ph3Co network on Au(111) at 4.5 K. STM parameters: V=-1 V, I=10 pA. (**C**) 30 nm x 30 nm STM image of Ph6Co network on Au(111) at 4.5 K. The Ph6Co hexagonal network grows 30° rotated from $[1\bar{1}0]$ direction of the surface. STM parameters: V= -0.5 V, I= 150 pA. (**D**) 80 nm x 80 nm STM long-range image of Ph6Co network on Au(111) at 4.5 K, highlighting its single domain and high quality. STM parameters: V= -0.5 V, I=10 pA. The compact high symmetry directions are indicated in **B** and **C**

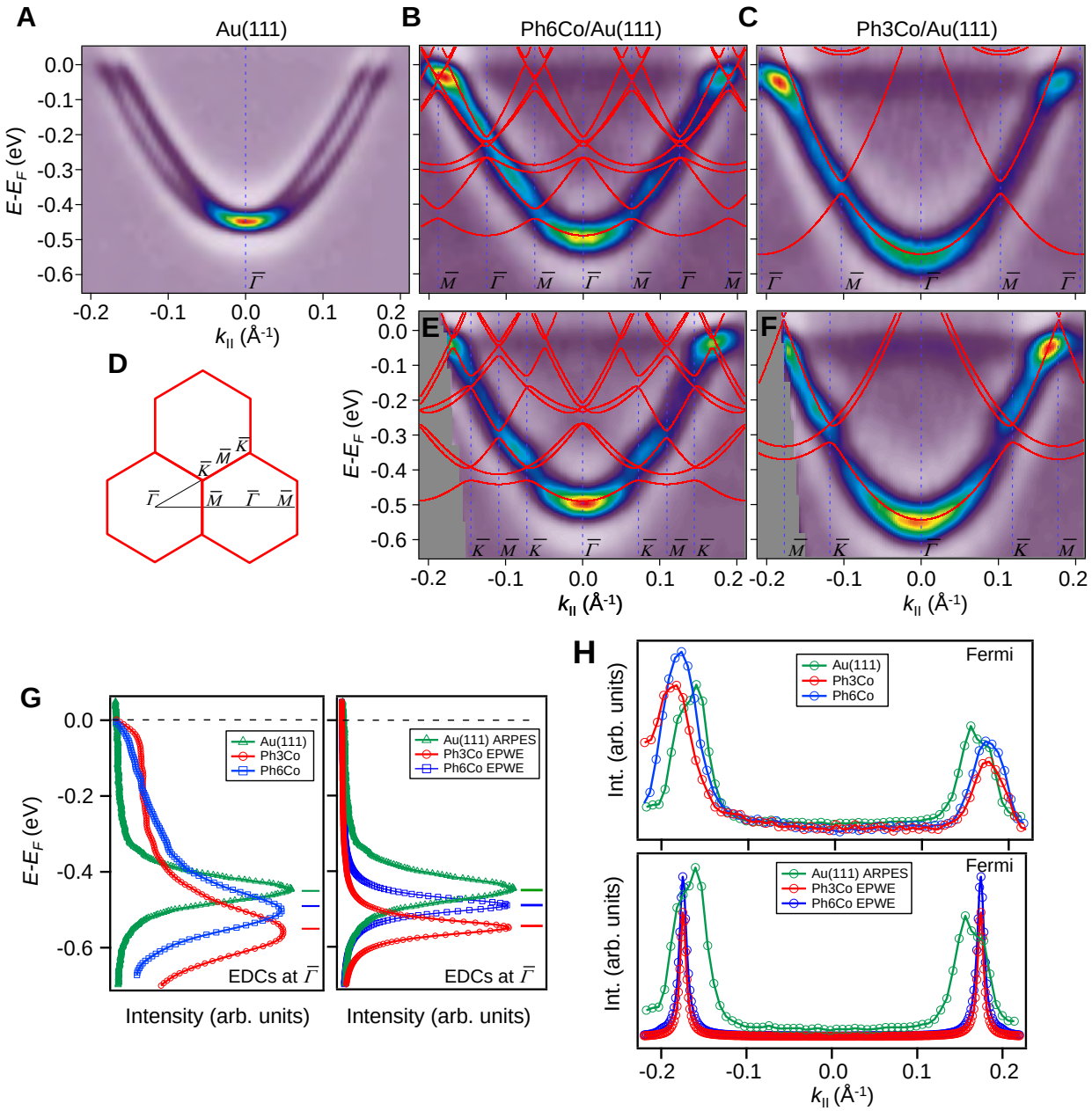

Figure S 2: ARPES and EPWE simulated electronic band structures, band bottom energies and Fermi wave-vector features. Second derivative electronic band structure of Au(111) SS (**A**), Ph6Co/Au [$\overline{\Gamma M}$ direction in (**B**) and $\overline{\Gamma K}$ in (**E**)] and Ph3Co/Au [$\overline{\Gamma M}$ direction in (**C**) and $\overline{\Gamma K}$ in (**F**)]. (**D**) Schematic representation of the surface Brillouin zone defined by Ph6Co and Ph3Co networks and the $\overline{\Gamma M}$ and $\overline{\Gamma K}$ high symmetry directions considered in ARPES. (**G**) A gradual shift of the band bottom energy towards lower energies is experimentally observed (left), the largest one being for the Ph3Co case, while for Ph6Co a smaller shift is detected. This tendency is satisfactorily matched by EPWE simulations (right). (**H**) Experimental (top) and EPWE simulated (bottom) Fermi wave-vector features are plotted for both Ph3Co (red) and Ph6Co (blue) networks and compared to the pristine Au surface state (green). Despite the large band bottom energy variations at $\overline{\Gamma}$, no population of the surface state is observed since the Fermi wave-vector remains pinned.

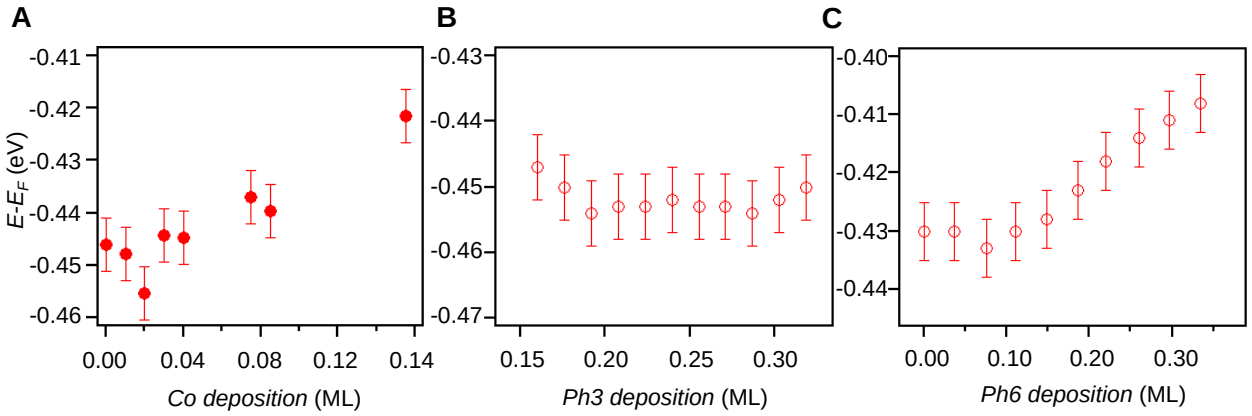

Figure S 3: Surface state energy variation upon Co, Ph3 and Ph6 gradient depositions. (**A**) The plot shows a tendency of the surface state to shift towards the Fermi level as the Co deposition is increased (likely due to Co clustering). For the diluted amount of Co required for both Ph3Co and Ph6Co network formations the surface state remains unaltered within the experimental error. (**B**) and (**C**) plots for Ph3 and Ph6 gradient depositions show that at low coverages the surface state remains energetically unchanged and gradually shifts towards the Fermi level, although it is more clearly observed for Ph6. The small energy variation at zero coverage for the Ph6 case is attributed to slight deviations from normal emission.

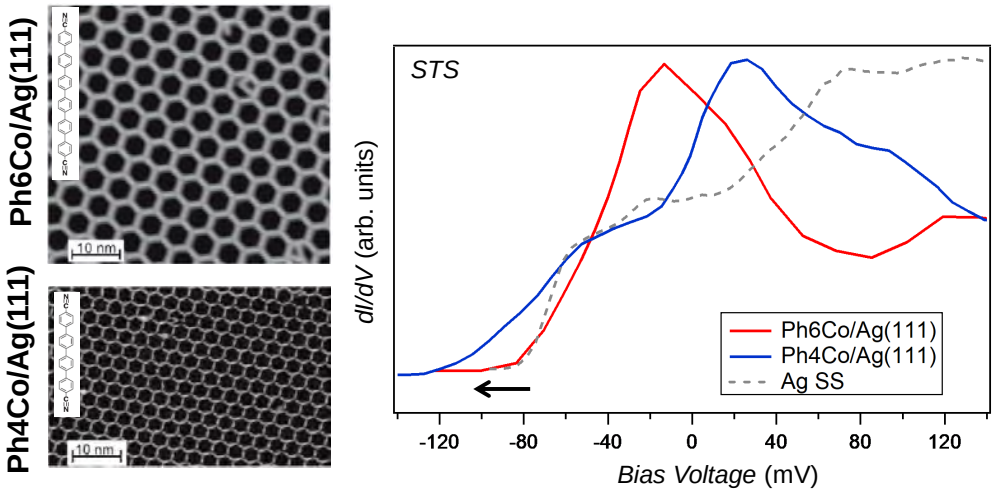

Figure S 4: Energy renormalization effects from dicarbonitrile-polyphenyl MONN on Ag(111). The left topographic images show two networks generated on Ag(111) when mixing with Co atoms the molecules Ph6 (top) and Ph4 (bottom) (shown in the insets). On the right, the different dI/dV spectra at the pore centers (Ph6Co in red and Ph4Co in blue) are compared to the pristine Ag(111) SS (dotted gray line) close to its energy onset (band bottom SS energy). Similarly to the Au(111) case, we observe a clear downshift of the onset energy, as indicated by the horizontal arrow, that is dependent on the Co adatom concentration, i.e. it is larger for Ph4Co. This figure has been adapted from Ref. [4].

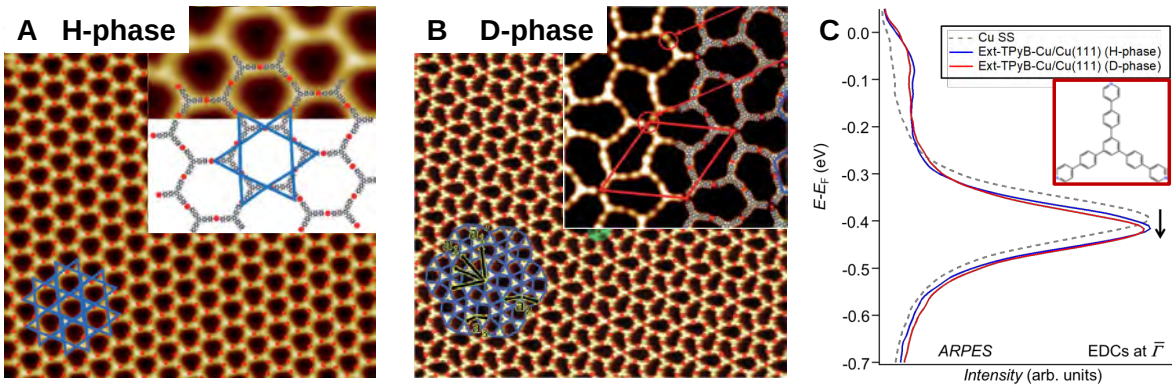

Figure S 5: Experimental confirmation of the downshift effect on two other MONNs with single metal coordination. (**A**) and (**B**) show topographic images of two ext-TPyB-Cu molecular networks generated on Cu(111) (adapted from [12]). In the H-phase (hexagonal network) the Cu adatoms coordinate with two adjacent molecules, whereas in the D-Phase we find two-fold and three-fold Cu-pyridyl coordination motifs. (**C**) ARPES EDCs at the $\overline{\Gamma}$ point (k=0) of the two MONNs. Compared with the pristine Cu(111) surface state (Cu SS, gray discontinuous line) we observe a 2DEG renormalization when these MONNs are present on the metal surface.

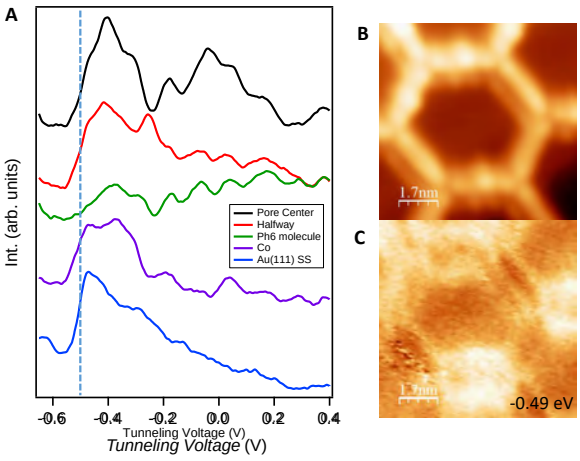

Figure S 6: Position dependent STS for Ph6Co and dI/dV map of a pore at the 2DEG onset. (**A**) The STS spectra discard the existance of bound states at the Co adatom since their expected features and corresponding modulation with distance are not visible in our dataset. Topography (**B**) and corresponding dI/dV map (**C**) for a Ph6Co pore at the 2DEG onset. At this energy the underlying herringbone reconstruction dominates the LDOS. Even if the STM data were taken with a slight double tip, no extra intensity is found at the Co adatoms with respect to the rest of the image. Note that the first confined resonance ($n = 1$) can only be visualized at higher voltages (see main text for details).

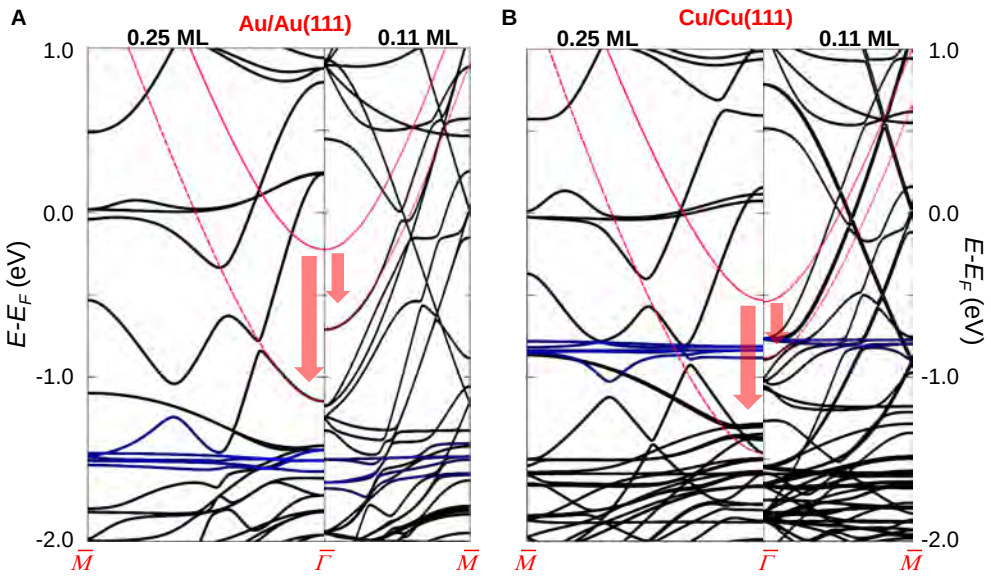

Figure S 7: Validation of the energy downshift of the 2DEG band bottom energy from homoatomic arrays grown on noble metal surfaces by means of DFT. The panels show the cases of (**A**) Au adatoms on Au(111) and (**B**) Cu adatoms on Cu(111) for 2x2 (0.25 ML) and 3x3 (0.11 ML) surface unit cells. Similarly to Fig. 3 of the main text, the hybridization between the pristine SS with the adatom d-bands (in blue) and the substrate's folded bulk bands open tiny gaps and pushes downwards the 2DEG (vertical arrows), the shift being larger for higher adatom coverages. We represent the pristine SS by a full red line and the altered one with a dotted line as a guide to the eye. This downshift found both for homoatomic and heteroatomic arrays turns out to be recurrent, as long as the SS character is maintained, i.e. the existing hybridizations are not strong.

SUPPLEMENTARY REFERENCES

[1] I. Piquero-Zulaica, S. Nowakowska, J. E. Ortega, M. Stöhr, L. H. Gade, T. A. Jung, and J. Lobo-Checa, Applied Surface Science **391**, 39 (2017).

[2] I. Horcas, R. Fernandez, J. M. Gomez-Rodriguez, J. Colchero, J. Gomez-Herrero, A. M. Baro, R. Fernández, J. M. Gómez-Rodríguez, J. Colchero, J. Gómez-Herrero, et al., Review of Scientific Instruments **78**, 013705 (2007).

[3] F. J. García de Abajo, J. Cordón, M. Corso, F. Schiller, and J. E. Ortega, Nanoscale **2**, 717 (2010).

[4] F. Klappenberger, D. Kühne, W. Krenner, I. Silanes, A. Arnau, F. J. García de Abajo, S. Klyatskaya, M. Ruben, and J. V. Barth, Physical Review Letters **106**, 026802 (2011).

[5] G. Kresse and J. Hafner, Phys. Rev. B **47**, 558 (1993).

[6] G. Kresse and J. Furthmüller, Physical Review B **54**, 11169 (1996).

[7] G. Kresse and J. Furthmüller, Computational Materials Science **6**, 15 (1996).

[8] J. P. Perdew, K. Burke, and M. Ernzerhof, Physical Review Letters **78**, 1396 (1997).

[9] N. Gonzalez-Lakunza, I. Fernández-Torrente, K. J. Franke, N. Lorente, A. Arnau, and J. I. Pascual, Physical Review Letters **100**, 156805 (2008).

[10] M. Ruiz-Osés, D. G. de Oteyza, I. Fernández-Torrente, N. Gonzalez-Lakunza, P. M. Schmidt-Weber, T. Kampen, K. Horn, A. Gourdon, A. Arnau, and J. E. Ortega, ChemPhysChem **10**, 896 (2009).

[11] J. I. Urgel, D. Écija, G. Lyu, R. Zhang, C.-A. Palma, W. Auwärter, N. Lin, and J. V. Barth, Nature Chemistry **8**, 657 (2016).

[12] L. Yan, G. Kuang, Q. Zhang, X. Shang, P. N. Liu, and N. Lin, Faraday Discuss. **204**, 111 (2017).